Shortening of microtubule overlap regions defines membrane delivery sites during plant cytokinesis

Jeroen de Keijzer[1,2], Henk Kieft[1], Tijs Ketelaar[1], Gohta Goshima[2,3], Marcel E. Janson[1,2 *]

[1] Laboratory of Cell Biology, Wageningen University, Droevendaalsesteeg 1, 6708 PB Wageningen, The Netherlands

[2] Marine Biological Laboratory, 7 MBL Street, Woods Hole, Massachusetts 02543, USA

[3] Division of Biological Science, Graduate School of Science, Nagoya University, Furo-cho, Chikusa-ku, Nagoya 464-8602, Japan

* To whom correspondence should be addressed: marcel.janson@wur.nl

Summary

Different from animal cells that divide by constriction of the cortex inwards, cells of land plants divide by initiating a new cell wall segment from their centre. For this, a disk-shaped, membrane-enclosed precursor termed the cell plate is formed that radially expands towards the parental cell wall [1–3]. The synthesis of the plate starts with the fusion of vesicles into a tubulo-vesicular network [4–6]. Vesicles are putatively delivered to the division plane by transport along microtubules of the bipolar phragmoplast network that guides plate assembly [7–9]. How vesicle immobilisation and fusion are then locally triggered is unclear. In general, a framework for how the cytoskeleton spatially defines cell plate formation is lacking. Here we show that membranous material for cell plate formation initially accumulates along regions of microtubule overlap in the phragmoplast of the moss *Physcomitrella patens*. Kinesin-4 mediated shortening of these overlaps at the onset of cytokinesis proved to be required to spatially confine membrane accumulation. Without shortening, the wider cell plate membrane depositions evolved into cell walls that were thick and irregularly shaped. Phragmoplast assembly thus provides a regular lattice of short overlaps on which a new cell wall segment can be scaffolded. Since similar patterns of overlaps form in central spindles of animal cells, involving the activity of orthologous proteins [10,11], we anticipate that our results will help uncover universal features underlying membrane-cytoskeleton coordination during cytokinesis.

Results and Discussion

Early ultrastructural work in the flowering plant *Haemanthus katherinae* has revealed that microtubules from the two halves of the phragmoplast interdigitate at the midplane where cell plate vesicles aggregate [12]. The same configuration exists in the phragmoplast of the moss *Physcomitrella patens* [13], indicating that it might be universally relevant for the spatial orchestration of cytokinesis in land plants. We therefore investigated whether regions of antiparallel microtubule overlap could have a direct role in determining the location of cell plate assembly in the genetically amenable moss *P. patens* (Figure 1A). For this we imaged the conserved microtubule bundling protein MAP65c labelled with citrine (a GFP variant) as a marker for microtubule overlaps [14–16] in combination with the lipophilic dye FM4-64 that stained the membrane of the forming cell plate in life caulonema apical cells (Figure 1A-B). Membranous material first became visible in the phragmoplast midplane approximately 2 minutes after the onset of anaphase (t = 0). At this stage cell plate membrane and overlap signals were momentarily strongly correlated and appeared as two coinciding punctate patterns at the midplane (Figure 1B; Movie S1). As the construction of the cell plate progressed, membranous material also became visible in between microtubule overlaps. Later, the initial microtubule overlaps disappeared, leaving behind a continuous plane of membranous material. Throughout cytokinesis, new overlaps showing isolated membrane association were formed at the phragmoplast periphery, expanding the structure radially [17]. It thus appeared that overlaps are platforms for the initial deposition of cell plate membrane at the start of cytokinesis and thereafter at the expanding edge of the phragmoplast. This warranted further investigation of their dynamics throughout cell division.

At anaphase onset, overlap regions of interpolar microtubules of the spindle apparatus decreased in length and closely coordinated their mutual positions onto a straight plane perpendicular to the spindle axis (Figure 1B). This shortening of overlaps has likewise been reported in higher plants and their limited length is maintained throughout cytokinesis [14,18]. To investigate whether length confinement of overlaps in the phragmoplast is a prerequisite to precisely define the position of membrane deposition, we sought a way to interfere with overlap length. To this end we investigated the functioning of kinesin-4 motor proteins, whose disruption causes a marked increase in overlap length in central spindles of animal cells, but for which no cytokinetic function has yet been attributed in plants [10,11,19]. Two *P. patens* kinesin-4 molecules, Kinesin4-Ia and Kinesin4-Ic (hereafter referred to as Kin4-Ia and Kin4-Ic), were observed at the phragmoplast midplane in a *P. patens* localization screen [20]. In our investigation, cells lacking both these kinesin-4 motors failed to shorten their overlaps at the start of anaphase and instead maintained long overlaps until the completion of cytokinesis (Figure 2A; Figure S1; Movie S2). Smaller defects present in the single mutants became particularly apparent when an average kymograph was constructed summarizing the overlap-dynamics of many cells (Figure 2B). Cells that only lacked Kin4-Ia showed mild extensions during late cytokinesis while overlap shortening was markedly delayed upon the sole removal of Kin4-Ic (Figure 2B, arrowheads). Interestingly, this delay corresponded in time with the late recruitment of Kin4-Ia onto cytokinetic overlaps (Figure S2A-B). Arrival of either motor was thus sufficient for overlap shortening. In addition to extended overlaps, we noted an absence of the

characteristic rotation of the division plane to an oblique orientation in the kinesin-4 double mutant (Figure 2A; Movie S2). Consequently, finalized cross walls in this mutant ran primarily perpendicular to the cell axis (Figure S2C-D). Whether kinesin-4 has a direct role in division plane reorientation is currently unclear because the underlying process is mechanistically not understood.

The mechanism by which kinesin-4 induces overlap shortening was investigated using a purified recombinant N-terminal fragment of moss Kin4-Ic. We observed that it supressed microtubule growth velocities in a dose dependent manner with a minimal effect on catastrophe rate (Figure S2E-H). The mode of action of kinesin-4 thus appeared to be conserved between animals and plants [21–23]. Recruitment of kinesin-4 onto phragmoplast overlaps may thus prevent their elongation by inhibiting the growth of microtubules within them. Shortening could then occur if microtubules simultaneously slide apart [10,11,22].

Having found a way to increase overlap length, we next examined the consequences for the accumulation of cell plate membrane. The practical usability of FM4-64 to visualize cell plate membranes was limited because staining, although bright, was variable and dye administration required precise timing, hampering quantitative comparison across many cells. We therefore labelled an endogenous integral membrane protein belonging to the secretory carrier membrane protein (SCAMP) family, which we designated SCAMP4 (Figure S3A-C). This protein localized to the plasma membrane, early endosomal compartments and the cell plate as described for SCAMPs of higher plants [24] (Figure S3D-E). We first inspected the expanding edge of the phragmoplast

where, as described above, cell plate material specifically accumulated at overlaps (Figure 1B). Compared to wild type cells, longer membrane-structures were visible along the extended overlaps of the Δ*kin4-Ia*/*Ic* mutant, but rarely did they encompass the entire overlap length (Figure 3A). Upon a closer inspection of the dynamics of the assembly process we noted that particularly long stretches of membrane material did occasionally form (Figure 3E; Movie S3). However, these readily coalesced into the cell plate even whilst the underlying overlaps were still intact. To assess whether this remodelling could eventually reduce the width of the cell plate to a wild-type level, we next analysed more mature parts of the cell plate where membrane material was also visible in between overlaps (Figure 3B). In the Δ*kin4-Ia*/*Ic* mutant, membrane material clearly aggregated near the centre of overlaps, but an overall widening of the cell plate remained notable (Figure 3B). Differences were verified by averaging line scans of SCAMP4 signals and determining the widths of their intensity distribution (Figure 3C-D; Figure S4A). A consistent widening of the cell plate in the kinesin-4 double mutant was also visible using DIC optics (Figure S4B-C). Taken together, confinement of the initial deposition of cell plate membrane through kinesin-4-mediated overlap length restriction is essential to control ultimate cell plate thickness.

Apart from the observed broadening of cell plates we also noticed a delayed progression of cytokinesis in cells lacking both kinesin-4s. Compared to wild type cells, the radial expansion velocity of the phragmoplast was halved in kinesin-4 double mutant cells (Figure 3F). Since expansion requires the continuous formation of new microtubule overlaps at the phragmoplast edge

[17], we hypothesized that kinesin-4 may have had a direct role in the formation of new overlaps. However, abundant overlap formation during expansion was still discernible in the mutant situation (Movie S4). Moreover, simultaneous imaging of Kin4-Ic and MAP65a demonstrated that overlaps became enriched with kinesin-4 only after they were formed (Figure S4D-E). We therefore favour an alternative scenario in which the expansion rate of the phragmoplast is coupled to the degree of maturation in the central part of the cell plate. The slower expansion in the kinesin-4 double mutant may then be explained by the initial wider deposition of membrane material requiring more time to be transformed into a coherent cell plate.

As the cell plate lumen becomes reinforced with various polysaccharides it gradually matures into a new cell wall segment [5,25]. The abnormalities in cell plate assembly arising from longer microtubule overlaps were thus expected to be reflected in the morphology of completed cross walls. Indeed, when observed using transmission electron microscopy, completed walls in kinesin-4 double mutants were irregularly shaped, thicker (1.32 ±0.32 μm (SD; n=23) against 0.46 ±0.13 μm (n=27) in wild type; $P<0.001$ in Students *t*-test) and showed an abnormal texture, often with visible inclusions (Figure 3G). Interestingly, mild structural defects were also observed in both kinesin-4 single mutants, highlighting that even a mild disruption of overlap length can ultimately result in improperly deposited walls (Figure S4F-G). It will be interesting to find out how the dwarfed phenotype of double mutant plants relates to the defective interface between neighbouring cells (Figure S1C). A key linking factor might be the permeability of plasmodesmata, which is known to affect signalling and

differential development among plant cells [26,27]. Channels of plasmodesmata appeared crooked in the kinesin-4 double mutant (Figure 3G, arrowheads). However, the consequence for intercellular transport remains to be investigated.

The classical view on cell plate assembly is that vesicles are transported along microtubules towards the phragmoplast midplane [1–3,7,8]. The polarized orientation of microtubules alone however does not explain why cell plate initials are only formed there [16]. With our current findings we propose a leading role for overlaps in spatially orchestrating vesicle immobilization and facilitating their localised fusion (Figure 4). How cell plate vesicles can become associated to these specific cytoskeletal structures is then a relevant question. We reasoned that vesicle transport may stall at overlaps if vesicle-associated motor proteins interact with microtubules of opposite polarity [28]. Alternatively, vesicles may diffuse passively and bind overlap-associated factors to accumulate locally. In both scenarios, the successive step of vesicle fusion possibly requires the recruitment of vesicle tethering and fusion machinery onto overlaps (Figure 4) [1,29–31]. It is highly conceivable that MAP65 plays a direct role in this based on recruitment-strategies in related bipolar microtubule networks [32,33]. Such a notion is also congruent with silencing of MAP65 in moss upon which membrane accumulation stalls during early cytokinesis and no uniform cell plate is formed [16]. We anticipate that the kinesin-4 mutants will be instrumental to further identify and understand the signalling pathways operating at the phragmoplast midplane.

For long it has been recognized that regions of microtubule overlap in animal central spindles and plant phragmoplasts form a highly regular lattice during cytokinesis [9,34]. Our results show that overlaps in an early divergent land plant are fine-tuned this way to precisely define a plane on which the cell plate is scaffolded. Overlaps therefore not only have a structural role in maintaining the bipolarity of the phragmoplast microtubule network [15,16,18,35–37], but provide a well-defined spatial signal for cell plate membrane aggregation and subsequent fusion. In dividing animal cells, microtubule overlaps of the central spindle concentrate signalling molecules to locally promote contractile ring formation and abscission [38–40]. A high degree of overlap organization therefore seems to be a common requirement for localizing cytokinetic machinery and the involvement of multiple conserved factors including MAP65 and kinesin-4 suggests that its necessity arose early in the evolution of the eukaryotic cell. The identification of overlaps as central players in phragmoplast functioning therefore does not only provide a framework for future work on plant cytokinesis, but provides means to discover common mechanisms in diverse cytokinetic networks that all share a role in the coordination of cytoskeletal and membrane-based processes.

Experimental Procedures

See Supplemental Experimental Procedures

Author Contributions

MEJ and JK conceived the research. JK, TK, GG and MEJ developed and designed the methodology of experiments and analysis. JK performed experiments and

analysis. HK prepared and observed transmission electron microscopy samples. MEJ and JK wrote the manuscript with input and comments from all other authors.

Acknowledgements

The MBL in Woods Hole (MA) is gratefully acknowledged for use of equipment. We thank Aniek Jongerius for help with the in vitro experiments, Ken Kosetsu for sharing MAP65-labelled moss lines and Kyowa Hakko Kogyo for kindly providing driselase. The work has been financially supported by HFSP grant RGP0026/2011 to MEJ and GG.

References

1. Boruc, J., and van Damme, D. (2015). Endomembrane trafficking overarching cell plate formation. Curr. Opin. Plant Biol. *28*, 92–98.
2. Staehelin, L.A., and Hepler, P.K. (1996). Cytokinesis in higher plants. Cell *84*, 821–824.
3. Müller, S., and Jürgens, G. (2015). Plant cytokinesis - No ring, no constriction but centrifugal construction of the partitioning membrane. Semin. Cell Dev. Biol. *53*, 10–18.
4. Schmiedel, G., Reiss, H.D., and Schnepf, E. (1981). Associations between membranes and microtubules during mitosis and cytokinesis in caulonema tip cells of the moss *Funaria hygrometrica*. Protoplasma *108*, 173–190.
5. Samuels, A.L., Giddings, T.H., and Staehelin, L.A. (1995). Cytokinesis in tobacco BY-2 and root tip cells: A new model of cell plate formation in higher plants. J. Cell Biol. *130*, 1345–1357.
6. Gu, X., and Verma, D.P. (1996). Phragmoplastin, a dynamin-like protein associated with cell plate formation in plants. EMBO J. *15*, 695–704.
7. Otegui, M.S., Mastronarde, D.N., Kang, B.H., Bednarek, S.Y., and Staehelin, L.A. (2001). Three-dimensional analysis of syncytial-type cell plates during endosperm cellularization visualized by high resolution electron tomography. Plant Cell *13*, 2033–2051.
8. Lee, Y.J., Giang, H.M., and Liu, B. (2001). A novel plant kinesin-related protein specifically associates with the phragmoplast organelles. Plant Cell *13*, 2427–2439.
9. Euteneuer, U., and Mcintosh, J.R. (1980). Polarity of midbody and phragmoplast microtubules. J Cell Biol. *87*, 509–515.

10. Kurasawa, Y., Earnshaw, W.C., Mochizuki, Y., Dohmae, N., and Todokoro, K. (2004). Essential roles of KIF4 and its binding partner PRC1 in organized central spindle midzone formation. EMBO J. *23*, 3237–3248.
11. Hu, C.K., Coughlin, M., Field, C.M., and Mitchison, T.J. (2011). KIF4 regulates midzone length during cytokinesis. Curr. Biol. *21*, 815–824.
12. Hepler, P.K., and Jackson, W.T. (1968). Microtubules and early stages of cell-plate formation in the endosperm of *Haemanthus katherinae* Baker. J. Cell Biol. *38*, 437–446.
13. Hiwatashi, Y., Obara, M., Sato, Y., Fujita, T., Murata, T., and Hasebe, M. (2008). Kinesins are indispensable for interdigitation of phragmoplast microtubules in the moss *Physcomitrella patens*. Plant Cell *20*, 3094–3106.
14. Müller, S., Smertenko, A., Wagner, V., Heinrich, M., Hussey, P.J., and Hauser, M-T. (2004). The plant microtubule-associated protein AtMAP65-3/PLE is essential for cytokinetic phragmoplast function. Curr. Biol. *14*, 412–417.
15. Gaillard, J., Neumann, E., van Damme, D., Stoppin-Mellet, V., Ebel, C., Barbier, E., Geelen D., and Vantard, M. (2008). Two microtubule-associated proteins of Arabidopsis MAP65s promote antiparallel microtubule bundling. Mol. Biol. Cell *19*, 4534–4544.
16. Kosetsu, K., de Keijzer, J., Janson, M.E., and Goshima, G. (2013). MICROTUBULE-ASSOCIATED PROTEIN65 is essential for maintenance of phragmoplast bipolarity and formation of the cell plate in *Physcomitrella patens*. Plant Cell *25*, 4479–4492.
17. Murata, T., Sano, T., Sasabe, M., Nonaka, S., Higashiyama, T., Hasezawa, S., Machida, Y., and Hasebe, M. (2013). Mechanism of microtubule array expansion in the cytokinetic phragmoplast. Nat. Commun. *4*, 1967.
18. Ho, C-M.K., Hotta, T., Guo, F., Roberson, R.W., Lee, Y-R.J., and Liu, B. (2011). Interaction of antiparallel microtubules in the phragmoplast is mediated by the microtubule-associated protein MAP65-3 in *Arabidopsis*. Plant Cell *23*, 2909–2923.
19. Kong, Z., Ioki, M., Braybrook, S., Li, S., Ye, Z-H., Lee, Y-R.J., Hotta, T., Chang, A., Tian, J., Wang, G., et al. (2015). Kinesin-4 functions in vesicular transport on cortical microtubules and regulates cell wall mechanics during cell elongation in plants. Mol. Plant *8*, 1011–1023.
20. Miki, T., Naito, H., Nishina, M., and Goshima, G. (2014). Endogenous localizome identifies 43 mitotic kinesins in a plant cell. Proc. Natl. Acad. Sci. USA *111*, E1053–E1061.
21. Bringmann, H., Skiniotis, G., Spilker, A., Kandels-Lewis, S., Vernos, I., and Surrey, T. (2004). A kinesin-like motor inhibits microtubule dynamic instability. Science *303*, 1519–1522.
22. Bieling, P., Telley, I.A., and Surrey, T. (2010). A minimal midzone protein module controls formation and length of antiparallel microtubule overlaps. Cell *142*, 420–432.
23. van der Vaart, B., van Riel, W.E., Doodhi, H., Kevenaar, J.T., Katrukha, E.A., Gumy, L., Benjamin, P., Bouchet, B.P., Grigoriev, I., Spangler, S.A., Yu, K.L., et al. (2013). CFEOM1-associated kinesin KIF21A is a cortical microtubule growth inhibitor. Dev. Cell *27*, 145–160.
24. Law, A.H.Y., Chow, C.M., and Jiang, L. (2012). Secretory carrier membrane proteins. Protoplasma *249*, 269–283.
25. Drakakaki, G. (2015). Polysaccharide deposition during cytokinesis:

Challenges and future perspectives. Plant Sci. *236*, 177–184.
26. Brunkard, J.O., Runkel, A.M., and Zambryski, P.C. (2015). The cytosol must flow: Intercellular transport through plasmodesmata. Curr. Opin. Cell Biol. *35*, 13–20.
27. Han, X., and Kim, J.Y. (2016). Integrating hormone- and micromolecule-mediated signaling with plasmodesmal communication. Mol Plant *9*, 46–56.
28. Derivery, E., Seum, C., Daeden, A., Loubéry, S., Holtzer, L., Jülicher, F., and Gonzalez-Gaitan, M. (2015). Polarized endosome dynamics by spindle asymmetry during asymmetric cell division. Nature *528*, 280–285.
29. Fendrych, M., Synek, L., Pecenková, T., Toupalová, H., Cole, R., Drdová, E., Nebesárová, J., Sedinová, M., Hála, M., Fowler, J.E., et al. (2010). The Arabidopsis exocyst complex is involved in cytokinesis and cell plate maturation. Plant Cell *22*, 3053–3065.
30. Rybak, K., Steiner, A., Synek, L., Klaeger, S., Kulich, I., Facher, E., Wanner, G., Kuster, B., Zarsky, V., Persson, S., et al. (2014). Plant cytokinesis is orchestrated by the sequential action of the TRAPPII and exocyst tethering complexes. Dev. Cell *29*, 607–620.
31. Steiner, A., Rybak, K., Altmann, M., McFarlane, H.E., Klaeger, S., Nguyen, N., Facher, E., Ivakov, A., Wanner, G., Kuster, B., et al. (2016). Cell cycle-regulated PLEIADE/AtMAP65-3 links membrane and microtubule dynamics during plant cytokinesis. Plant J. *88*, 531–541.
32. Lee, K.Y., Davies, T., and Mishima, M. (2012). Cytokinesis microtubule organisers at a glance. J. Cell Sci. *125*, 3495–3500.
33. Duellberg, C., Fourniol, F.J., Maurer, S.P., Roostalu, J., and Surrey, T. (2013). End-binding proteins and Ase1/PRC1 define local functionality of structurally distinct parts of the microtubule cytoskeleton. Trends Cell Biol. *23*, 54–63.
34. Otegui, M.S., Verbrugghe, K.J., and Skop, A.R. (2005). Midbodies and phragmoplasts: analogous structures involved in cytokinesis. Trends Cell Biol. *15*, 404–413.
35. Janson, M.E., Loughlin, R., Loïodice, I., Fu, C., Brunner, D., Nédélec, F.J., and Tran, P.T. (2007). Crosslinkers and motors organize dynamic microtubules to form stable bipolar arrays in fission yeast. Cell *128*, 357–368.
36. Subramanian, R., Wilson-Kubalek, E.M., Arthur, C.P., Bick, M.J., Campbell, E.A., Darst, S.A., Milligan, R.A., and Kapoor, T.M. (2010). Insights into antiparallel microtubule crosslinking by PRC1, a conserved nonmotor microtubule binding protein. Cell *142*, 433–443.
37. de Keijzer, J., Mulder, B.M., and Janson, M.E. (2014). Microtubule networks for plant cell division. Syst. Synth. Biol. *8*, 187–194.
38. Wheatley, S.P., and Wang, Y.L. (1996). Midzone microtubule bundles are continuously required for cytokinesis in cultured epithelial cells. J. Cell Biol. *135*, 981–989.
39. Green, R.A., Paluch, E., and Oegema, K. (2012). Cytokinesis in animal cells. Annu. Rev. Cell Dev. Biol. *28*, 29–58.
40. Lekomtsev, S., Su, K-C., Pye, V.E., Blight, K., Sundaramoorthy, S., Takaki, T., Collinson, L.M., Cherepanov, P., Divecha, N., and Petronczki, M. (2012). Centralspindlin links the mitotic spindle to the plasma membrane during cytokinesis. Nature *492*, 276–279.

Figure Legends

Figure 1 Early cytokinetic membrane accumulation occurs at sites of microtubule overlap. (A) Schematic representation of cell plate formation in a dividing *P. patens* caulonemal tip cell and definition of the terminology used. MAP65 resides in between interdigitating microtubules in the phragmoplast midplane. An enlarged view of the boxed area is shown on the right. Arrows indicate direction of radial expansion. Not drawn to scale. (B) Snapshots of a dividing caulonemal tip cell expressing MAP65c-citrine stained with FM4-64 membrane dye. A single confocal plane is depicted. Time with respect to anaphase onset (t=0) is indicated in min:sec. Dashed lines indicate the cell boundary and arrowheads mark the midplane along which the depicted sideviews were generated. Magnified views of the areas indicated with the square brackets are shown. Here, the arrowheads highlight the punctate cell plate membrane accumulations that colocalized with a MAP65 labelled region of overlap. The Pearson correlation coefficient (R) between the MAP65 and FM4-64 signal intensities within the midplane is indicated on the right. Scalebars represent 5 μm, except for the magnified areas where 1 μm is indicated. See also Movie S1 which includes colour overlays of the two channels.

Figure 2 Two kinesin-4's jointly limit microtubule overlap length in the phragmoplast midplane. (A) Caulonemal tip cells expressing MAP65a-citrine and lacking Kin4-Ia and/or Kin4-Ic imaged throughout cell division. Dashed lines indicate the cell boundary. The time with respect to anaphase onset (t=0) is indicated in min:sec on the left. Images are maximum z-projections of 3 confocal planes spaced 0.5 µm apart. Scalebar indicates 5 µm. See also Figure S1, Figure S2 and Movie S2. (B) Evolution of the width of MAP65a-labeled overlaps throughout cell division shown by a kymograph for wild-type (average of n=7 cells), Δ*kin4-Ia* (n=9), Δ*kin4-Ic* (n=9) and Δ*kin4-Ia* / Δ*kin4-Ic* (n=9). Per time point, the normalized intensity distribution perpendicular to the midplane is shown after undulations in the midplane were straightened out computationally. Kymographs were limited to only contain information from at least half of the imaged cells. Arrowheads mark the slight overlap extension in the Δ*kin4-Ia* mutant and the delay in overlap compaction after anaphase onset in the Δ*kin4-Ic* mutant. Horizontal scalebar indicates 1 µm and vertical scalebar 5 minutes.

Figure 3 Broadened membrane deposition upon overlap overextension hampers cell plate assembly. (A) Early membrane accumulation analysed in single confocal planes acquired at the phragmoplast expansion site for dividing wild-type and Δ*kin4-Ia* / Δ*kin4-Ic* cells. MAP65-labelled overlaps and cell plate membranes visualized using SCAMP4-mCherry are shown. The location of the depicted confocal planes is illustrated at the top. Scalebar indicates 5 μm. See also Figure S3. (B) Cell plate membrane distribution analysed in the central plane corresponding to a site of more advanced cell plate maturation, visualized as described in A. (C) Spatial distribution profile of early cell plate membrane accumulation measured perpendicular to the division plane using the average SCAMP4-mCherry signal intensity in wild-type and Δ*kin4-Ia* / Δ*kin4-Ic* cells. The peak intensities were centered at 0 μm for individual cells before averaging. See also Figure S4A-C. (D) Distribution of cell plate membranes in the central plane measured as described in C. (E) Dynamics of membrane remodelling at overlap sites visualized in a Δ*kin4-Ia* / Δ*kin4-Ic* mutant cell expressing MAP65a-citrine and stained with FM4-64 to label membranes of the cell plate. A detailed view of the boxed area is shown in inverted contrast. Arrows point to elongated stretches of membrane associated with overlaps. The arrowheads point to an incident in which a stretch clearly coalesced into the forming cell plate. Images are maximum z-projections of 2 confocal planes spaced 0.5 μm apart. Scalebar indicates 5 μm in the overview image and 1 μm in the enlarged views. See also Movie S3. (F) Radial phragmoplast expansion velocities in wild-type and kinesin-4 deficient cells. Individual measurements for n≥10 cells and their medians are shown. ** indicates differences supported with P<0.001 in Students *t*-test. See also Figure S4D-E and Movie S4. (G) Transmission electron micrographs of cross

walls in wild type and the Δ*kin4-Ia* / Δ*kin4-Ic* mutant. An enlarged view of the boxed areas is shown on the right. Arrowheads indicate plasmodesmata, which appear crooked in the mutant cell wall. Scalebars indicate 5 μm in the left images and 500 nm in the enlarged views. See also Figure S4F-G.

Figure 4 Diagram of the successive steps in cell plate assembly and disruption thereof upon kinesin-4 removal. Under wild-type circumstances (left), after the formation of a region of antiparallel overlap involving MAP65 crosslinkers (yellow), kinesin-4 is recruited to limit overlap length. This in turn confines the initial cell plate membrane deposition to a well-defined plane. From our light microscopic observations it is unclear whether the transformation of vesicles into larger membrane structures, involving tethering and fusion, occurs at overlaps or in their direct vicinity. Initial membrane structures are remodelled and further maturation of the cell plate is achieved through deposition of cell wall polysaccharides [6,25]. In absence of kinesin-4 inhibitors of microtubule growth (right) elongated overlaps widen the zone of initial membrane deposition. Compared to wild type, this wide deposition is remodelled into a thicker cell plate at a greatly impaired rate.

Figure 1

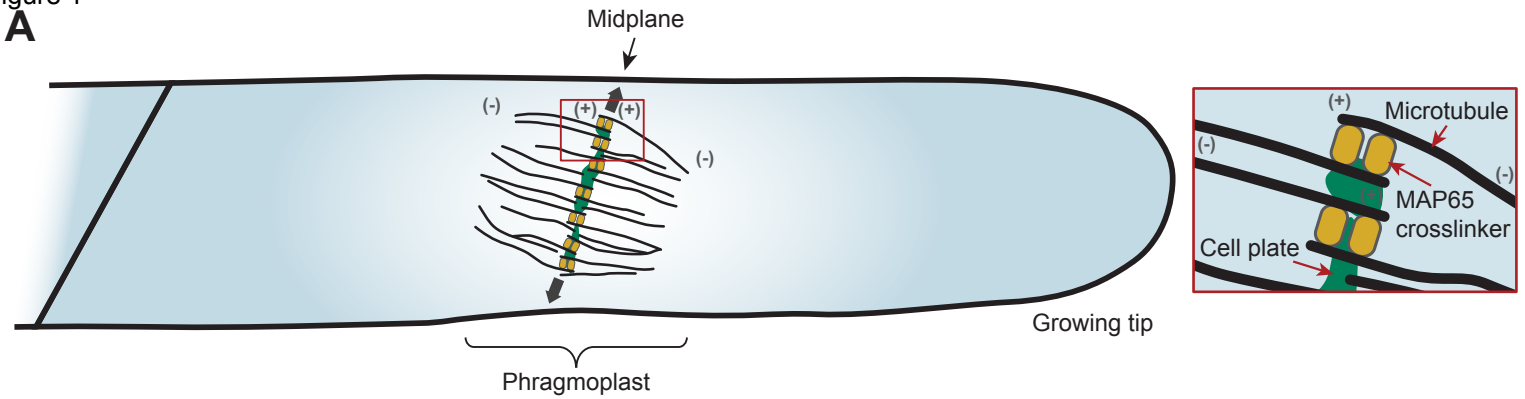
A
Midplane
(-)
(+)
(+)
(-)
Growing tip
Phragmoplast
(+)
Microtubule
(-)
(-)
MAP65
crosslinker
Cell plate

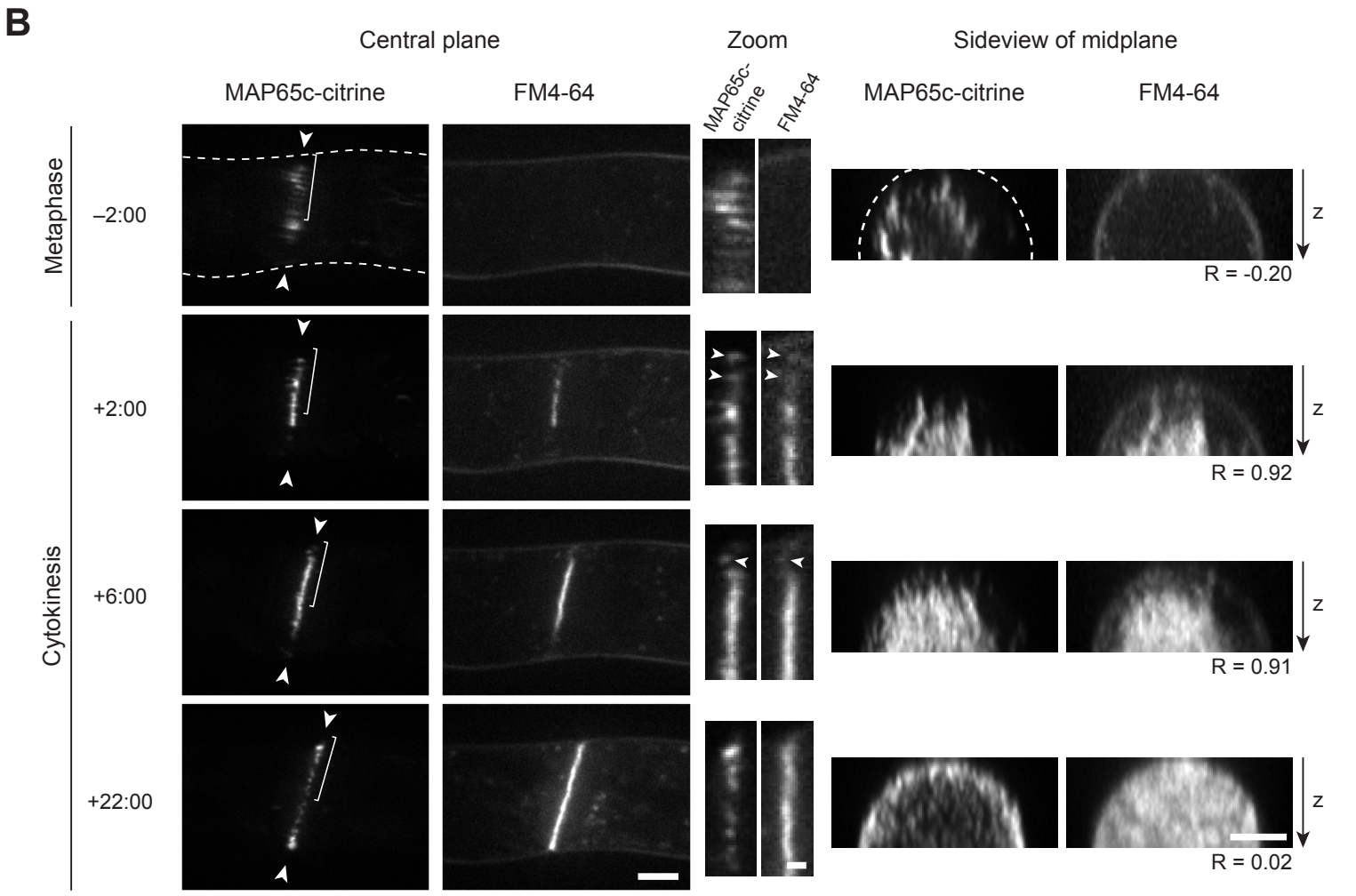
B
Central plane
Zoom
Sideview of midplane
MAP65c-citrine
FM4-64
MAP65c-citrine
FM4-64
MAP65c-citrine
FM4-64
Metaphase
Cytokinesis
–2:00
+2:00
+6:00
+22:00
z
R = -0.20
R = 0.92
R = 0.91
R = 0.02

Figure 2

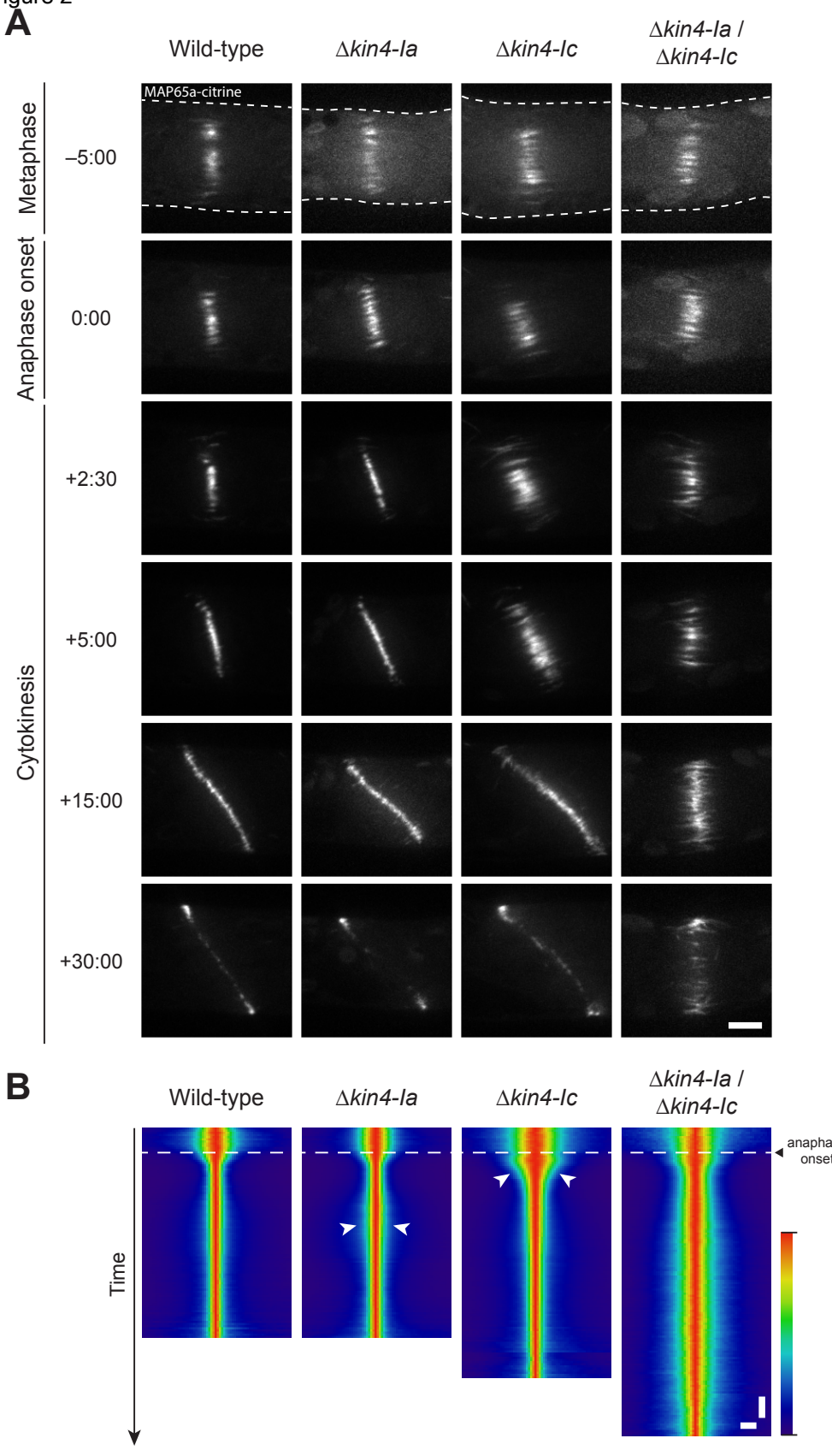
A
Wild-type
Δkin4-Ia
Δkin4-Ic
Δkin4-Ia / Δkin4-Ic
MAP65a-citrine
Metaphase
Anaphase onset
Cytokinesis
–5:00
0:00
+2:30
+5:00
+15:00
+30:00
B
Wild-type
Δkin4-Ia
Δkin4-Ic
Δkin4-Ia / Δkin4-Ic
anaphase onset
Time

Figure 3

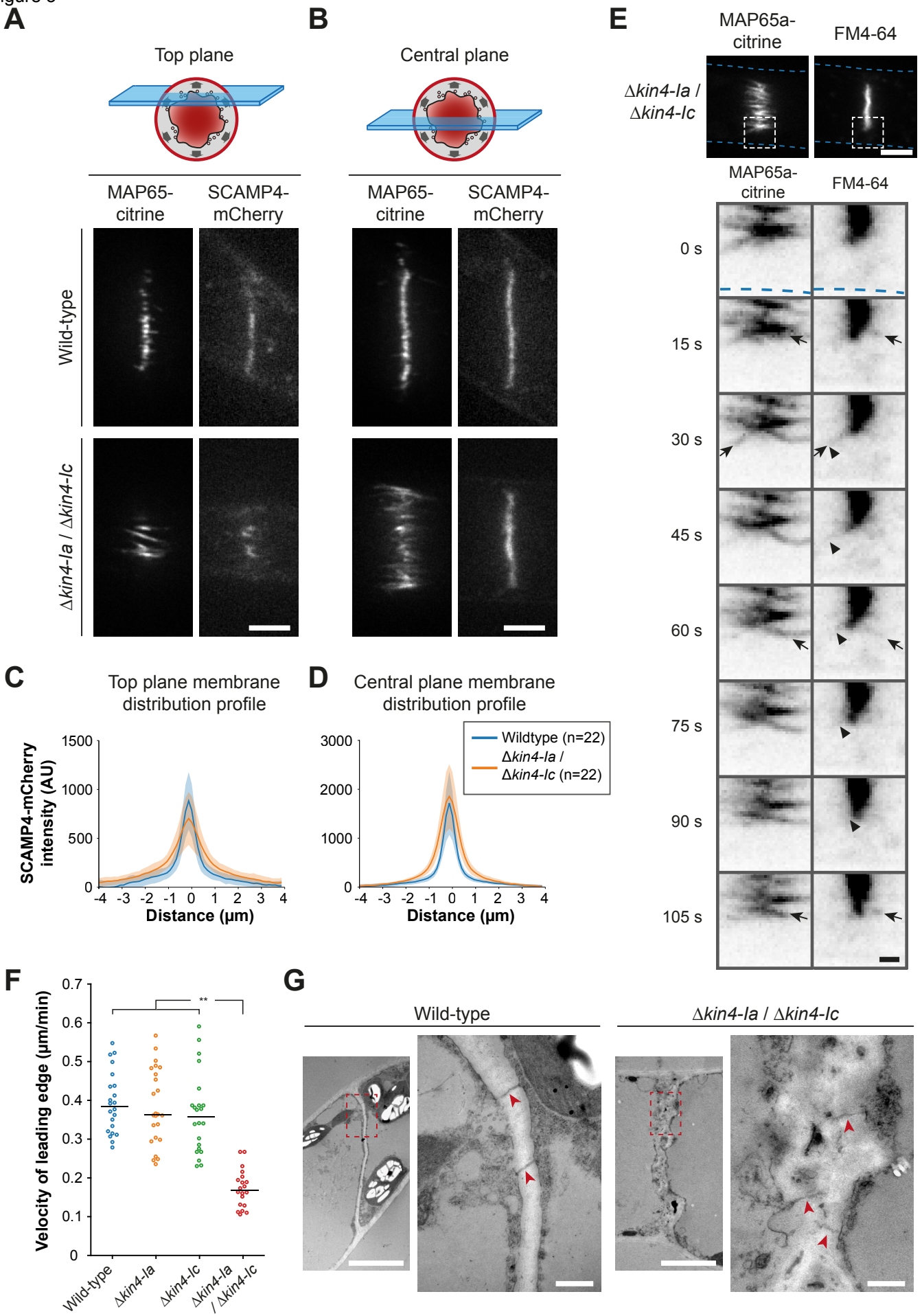
A
Top plane
Central plane
MAP65-citrine
SCAMP4-mCherry
Wild-type
Δkin4-Ia / Δkin4-Ic
B
C
Top plane membrane distribution profile
SCAMP4-mCherry intensity (AU)
Distance (μm)
D
Central plane membrane distribution profile
Wildtype (n=22)
Δkin4-Ia / Δkin4-Ic (n=22)
E
MAP65a-citrine
FM4-64
0 s
15 s
30 s
45 s
60 s
75 s
90 s
105 s
F
Velocity of leading edge (μm/min)
Wild-type
Δkin4-Ia
Δkin4-Ic
Δkin4-Ia / Δkin4-Ic
G
Wild-type
Δkin4-Ia / Δkin4-Ic

Figure 4

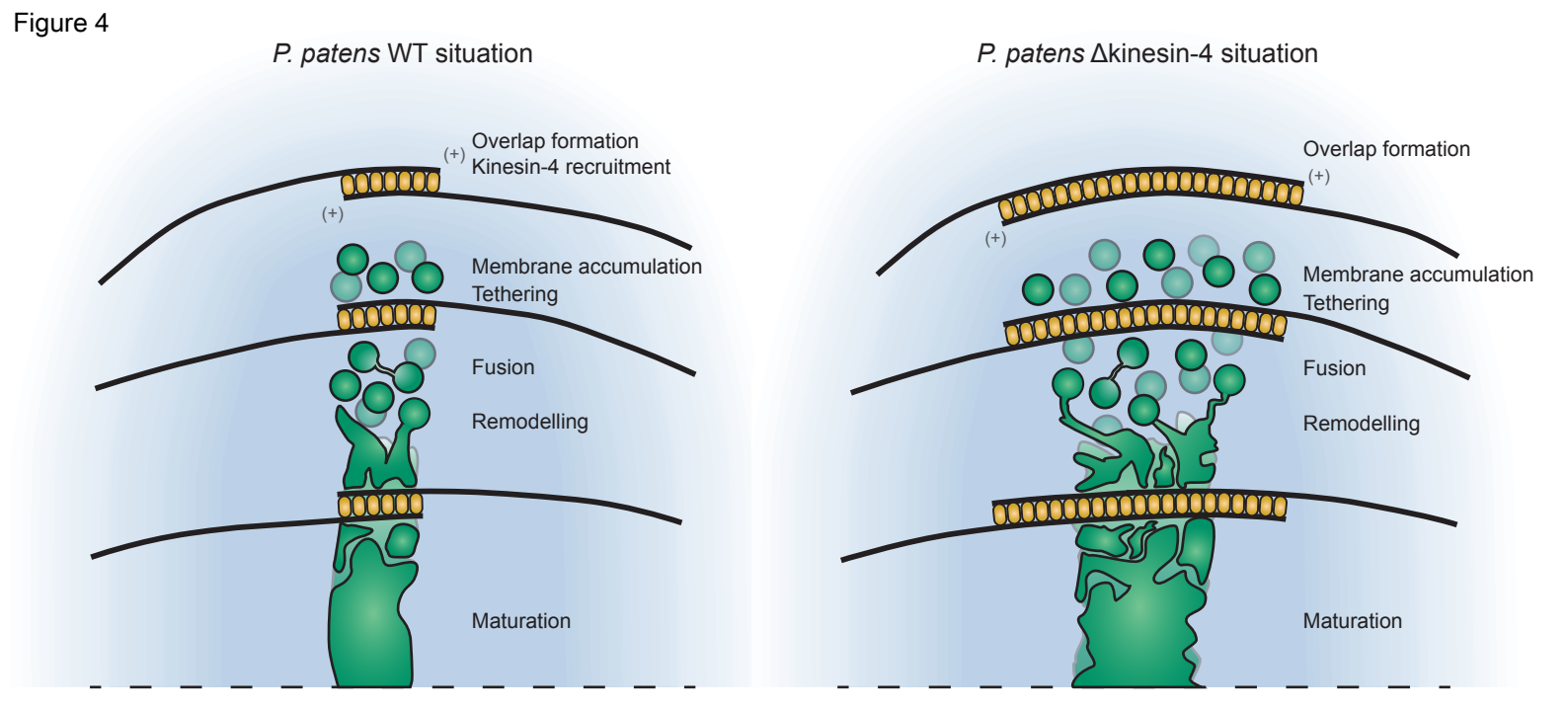
P. patens WT situation
Overlap formation
Kinesin-4 recruitment
(+)
(+)
Membrane accumulation
Tethering
Fusion
Remodelling
Maturation
P. patens Δkinesin-4 situation
Overlap formation
(+)
(+)
Membrane accumulation
Tethering
Fusion
Remodelling
Maturation

Supplemental Movie Legends

Movie S1 (Related Figure 1B) Timelapse movie of a dividing caulonemal tip cell expressing MAP65c-citrine stained with FM4-64 membrane dye. A single confocal plane taken at the cell centre is depicted at the top. A calculated sideview of the midplane is shown below. Time with respect to anaphase onset (t=0) is indicated in min:sec. Scalebars represent 5 µm.

Movie S2 (Related to Figure 2A) Timelapse movie of MAP65a-citrine labelled overlaps imaged throughout cell division in wild-type cells and cells lacking Kin4-Ia, Kin4-Ic or both. Dashed lines in the first frame of the movie indicate cell boundaries. Time with respect to anaphase onset (t=0) is indicated in min:sec. Scalebars represent 5 µm.

Movie S3 (Related to Figure 3E) Cell plate membrane dynamics at overlap sites visualized in a Δ*kin4-Ia* / Δ*kin4-Ic* mutant cell. Overlaps were visualized using MAP65a-citrine and FM4-64 was used to label cell plate membrane. Elongated membrane stretches transiently associated along overlaps to coalesce into the downwardly expanding cell plate. Images are maximum z-projections of 2 confocal planes spaced 0.5 µm apart. Dashed lines in the first frame of the movie indicate cell boundaries. Scalebar represents 1 µm.

Movie S4 (Related to Figure 3F) Timelapse movies of cell plate formation and expansion in wild-type and Δ*kin4-Ia* / Δ*kin4-Ic* mutant cells. Cells expressed citrine labelled MAP65a or MAP65c to visualize overlaps and SCAMP4-mCherry to label the membrane of the forming cell plate. Scalebar indicates 5 µm.

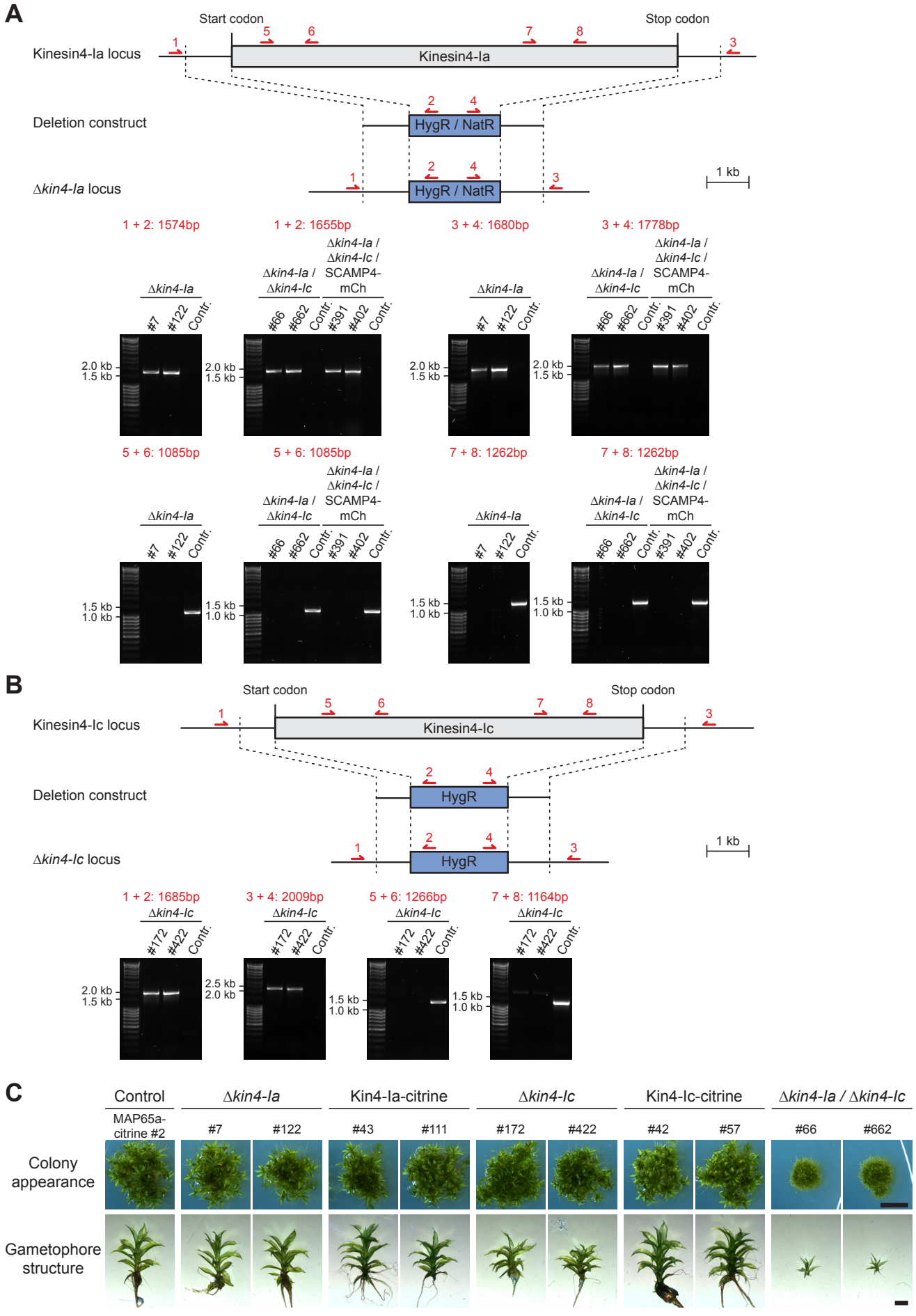

Figure S1 (Related to Figure 2) Generation, confirmation and appearance of Kinesin-4 deletion mutants. (A) Schematic representation of the genomic locus containing the Kin4-Ia encoding gene (gray box). Introduction of the deletion construct by homologous recombination

(dashed lines) led to replacement of the gene with a hygromycin or nourseothricin resistance cassette (blue box). Red arrows denote primer binding sites used for confirmation of the obtained lines. The products obtained after PCR reactions using different primer pairs and their predicted sizes are given below. Two independent transformants were tested per line. (B) Schematic of deletion of the Kin4-Ic encoding gene, similar as described in A. (C) Colony and gametophore appearance of moss lines in which Kin4-Ia and/or Kin4-Ic were absent or labelled with citrine. For each moss line two independent transformants are shown. Kin4-Ia deletion mutants and Kin4-Ia citrine-labelled lines exhibited no aberrant colony appearance. Albeit similar in size, colonies of Kin4-Ic deletion lines produced stunted gametophores. No such defects were present in lines expressing Kin4-Ic-citrine, strongly suggesting this is a functional fusion protein. Lines in which both Kinesin-4's were absent showed a reduced colony diameter and gametophores of severely reduced stature. Plants were photographed after 5 weeks of growth on BCD agar plates. The assay was repeated with similar outcomes. The scalebars represent 5 mm and 1 mm in the top and bottom rows respectively.

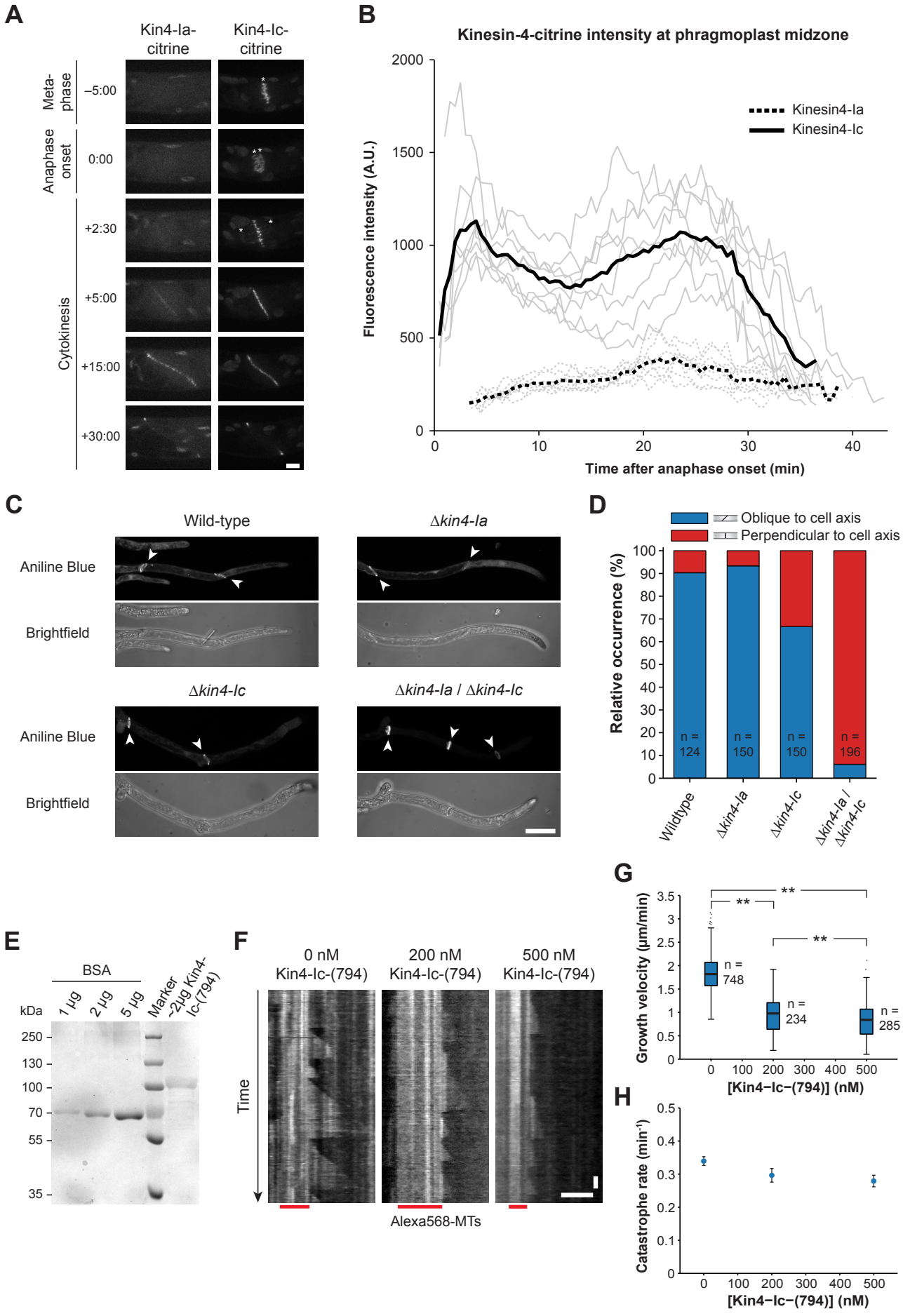

Figure S2 (Related to Figure 2) Differential arrival of kinesin-4s at the phragmoplast midplane, division plane rotation defects in absence of kinesin-4s and *in vitro* microtubule growth inhibition by Kinesin4-Ic. (A) Localization dynamics during cell division in cells with

endogenous Kin4-Ia or Kin4-Ic labelled with citrine. Kin4-Ic localized to chromosomes (marked with an asterix) and rapidly transferred to the phragmoplast midplane at anaphase onset. In contrast, Kin4-Ia was absent from chromosomes and was gradually recruited onto the midplane from the cytosol about 5 minutes after anaphase onset onwards. Shown images are maximum z-projections of 3 confocal planes spaced 0.5 µm apart. Scalebar indicates 5 µm. (B) Intensities of citrine-labelled Kin4-Ia and Kin4-Ic measured within the midplane throughout cytokinesis. Pixels of the midplane were isolated from the remainder of the image using an intensity threshold calculated using the maximum entropy method. The background signal measured in the cytosol was subtracted from the recorded intensities. For both proteins, profiles for 8 cells are shown together with their average value. All analysed cells were imaged with identical illumination and detection settings. (C) Cross wall orientation in kinesin-4 mutants visualized using Aniline Blue staining. The arrowheads mark the callose-rich cross walls. Images are maximum z-projections of 20 planes spaced 1.5 µm apart. Scalebar indicates 50 µm. (D) Relative occurrence of oblique and perpendicular cross walls in caulonema of kinesin-4 mutants as judged by eye. The indicated number of cross walls were scored in the apical and first two subapical caulonema cells of Aniline Blue stained tissue. The tissue was grown on BCD agar plates overlaid with cellophane. (E) Purified Kin4-Ic-(794) protein detected as a single band of approximately the expected size of 89.82 kDa on a coomassie-stained SDS-PAGE gel. Different amounts of BSA were loaded for densitometry. (F) Kymographs depicting microtubule growth initiated from stabilized seeds in presence of the indicated amount of purified Kin4-Ic-(794). Microtubules were visualized using Alexa568-tubulin. The slightly brighter labelled seed section is indicated below with a red bar. The horizontal scalebar represents 5 µm, the vertical scalebar 1 min. (G) Boxplots of microtubule growth velocity in presence of different amounts of Kin4-Ic-(794). The whiskers indicate minimum / maximum observed values or 1.5 times the interquartile range when outliers were present. The indicated number of growth events were analysed for each condition in at least 2 independent experiments. ** indicates differences that were supported with $P<0.001$ in Mann-Whitney U and Kruskal-Wallis tests. (H) Catastrophe rates plotted for different amounts of Kin4-Ic-(794). The total time microtubules were observed to spend in growth was at least 700 min for each condition.

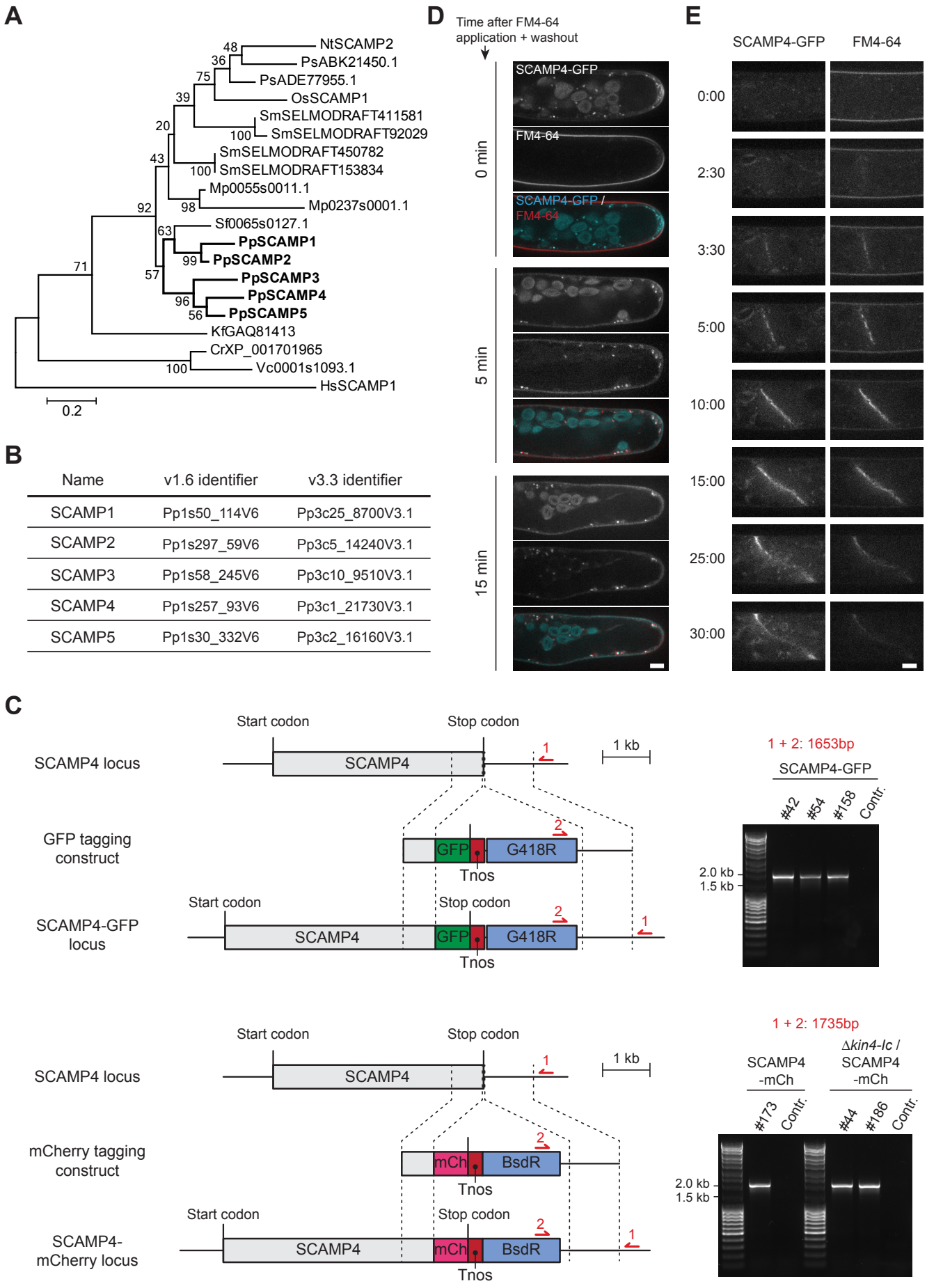

Figure S3 (Related to Figure 3A-D) Generation and validation of a labelled moss secretory carrier membrane protein (SCAMP) as cell plate membrane marker. (A) Phylogenetic tree of SCAMPs in non-flowering plants inferred using the maximum likelihood method. The included rice and tobacco SCAMPs have established cell plate localization [S1]. Human SCAMP1 served as an outgroup. Bootstrap

values (derived from 500 replicates) indicate the percentage of trees in which the associated taxa clustered together. Horizontal branch length represents the number of amino acid substitutions per site. Hs – *Homo sapiens*, Vc – *Volvox carteri*, Cr – *Chlamydomonas reinhardtii*, Kf – *Klebsormidium flaccidum*, Pp – *Physcomitrella patens*, Sf – *Sphagnum fallax*, Mp – *Marchantia polymorpha*, Sm – *Selaginella moellendorffii*, Os – *Oryza sativa*, Ps – *Picea sitchensis*, Nt – *Nicotiana tabacum*. The names used for the *Volvox*, *Sphagnum*, and *Marchantia* proteins are their Phytozome locus identifiers and the names used for *Chlamydomonas*, *Klebsormidium*, *Selaginella* and *Picea* proteins are their NCBI protein accession numbers. (B) Table listing cosmoss.org locus identifiers for the five SCAMP proteins encoded by the *Physcomitrella patens* genome using formatting of the indicated version of the genome assembly. (C) Schematic representation of the genomic locus containing the SCAMP4 encoding gene (gray box) and constructs used for C-terminal GFP and mCherry tagging via homologous recombination (dashed lines). In SCAMP4-labelled lines, the original stop codon is replaced with a fragment containing the GFP or mCherry encoding sequence (green and pink boxes respectively), the nopaline synthase terminator (red box) and a cassette conferring G418 or blasticidin resistance (blue box). Red arrows denote primer binding sites used for confirmation of the obtained lines. The product obtained after PCR reaction and its predicted size are given on the right. Despite a number of tested primers and PCR-conditions, integration of the left targeting arm could not be validated. The numbers of independently obtained transformants are given above the gel images. (D) Interphase protonemal cells expressing SCAMP4-GFP treated with FM4-64 in a pulse-chase experiment. Images show three different cells imaged at the indicated time after FM4-64 application and washout. The colocalization observed after 5 minutes indicated SCAMP4 resides at an early endosomal endomembrane compartment, presumably the trans-Golgi network [S1]. A single confocal plane from the cell centre is shown. The scalebar indicates 5 μm. (E) Dual localization of SCAMP4-GFP and FM4-64 in a dividing caulonemal cell. From the first arrival of vesicles ~3 minutes after anaphase onset (t=0) onwards, the cell-plate is similarly labelled by both markers. A single confocal plane is shown. The scalebar indicates 5 μm.

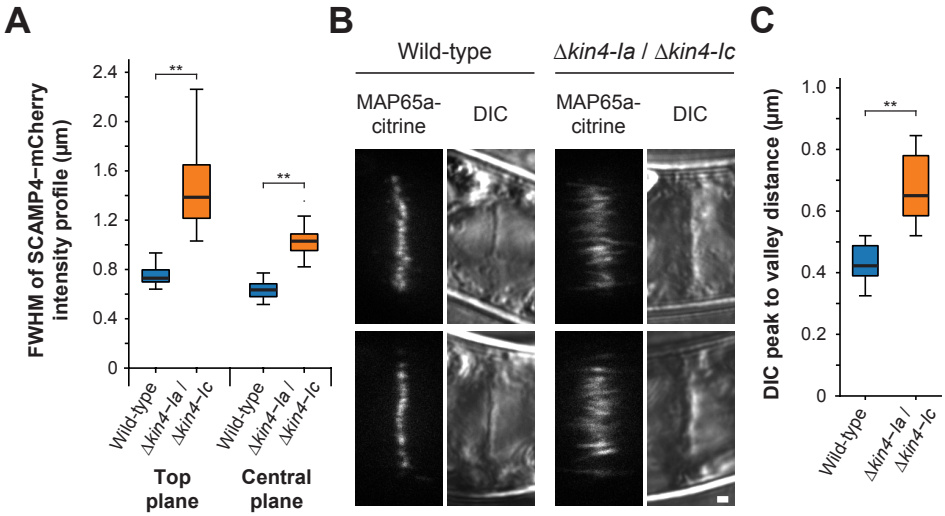

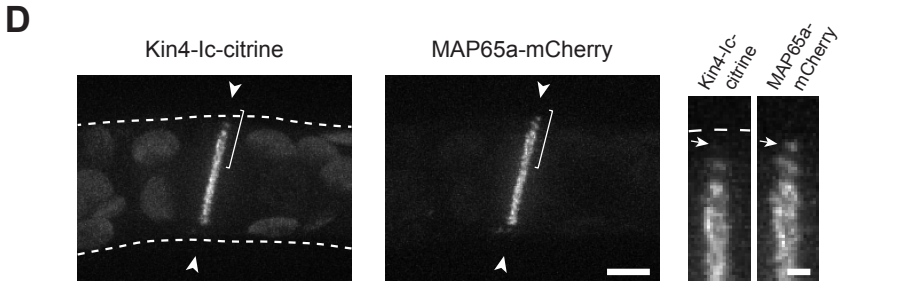

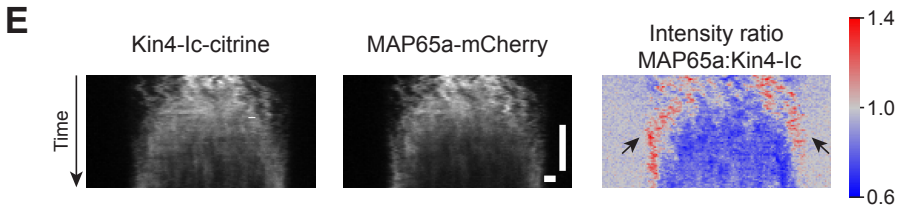

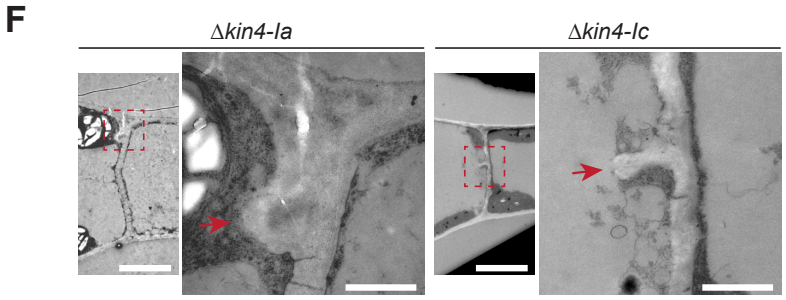

G

	Wild-type	Δ*kin4-Ia*	Δ*kin4-Ic*	Δ*kin4-Ia* / Δ*kin4-Ic*
Cross walls observed	27	18	34	23
Walls with defect in central region	1	2	11	23
Walls with defect at junction	1	5	6	23

Figure S4 (Related to Figure 3) Quantification of cell plate thickening, delayed enrichment of Kinesin-4 at overlaps during phragmoplast expansion and cross wall defects in Kinesin-4 mutants. (A) (Related to Figure 3C-D) Boxplots of the full width at half maximum (FWHM) of the SCAMP4-mCherry intensity distribution perpendicular to the cell plate at top and central confocal planes in wild-type (n=22) and Δ*kin4-Ia* / Δ*kin4-Ic* (n=22) cells. The whiskers indicate minimum / maximum observed values or 1.5 times the interquartile range when outliers were present. ** indicates differences that were supported with P<0.001 in Mann-Whitney U and Kruskal-Wallis tests. (B) Cell plates of wild-type and kinesin-4 knockout cells observed using differential interference contrast (DIC) microscopy. Corresponding confocal images of the MAP65a-citrine signal are shown on the left. Single optical sections taken at ~3 µm from the phragmoplast edge for two cells per genotype are shown. Scalebar indicates 1 µm. (C) Boxplots of the distance of the bright region on one side of the cell plate (peak) to the dark region on the opposite side (valley) obtained from DIC images of cell plates in wild-type (n=12) and Δ*kin4-Ia* / Δ*kin4-Ic* (n=15) cells. Distances were measured using a linescan of a 1 µm wide line segment oriented perpendicular to the cell plate.

(D) (Related to Figure 3F) Still image of a radially expanding phragmoplast (~4 min after anaphase onset) with endogenous Kin4-Ic and MAP65a labelled. A magnified view of the bracketed area shows MAP65a-positive overlaps at the expanding edge with little Kin4-Ic present. Arrowheads indicate the line used for generation of the kymographs shown in E. The image is a maximum projection of 5 planes acquired with 0.5 μm spacing. Scalebar represents 5 μm and 1 μm in the enlarged views. (E) Kymographs for Kin4-Ic-citrine and MAP65a-mCherry in the phragmoplast midplane indicated in D. The ratio between the two signals is represented on the right. At the two expanding phragmoplast edges (indicated with arrows) a relative deficiency of Kin4-Ic is apparent, while otherwise the Kin4-Ic signal is equal to, or exceeding that of MAP65. Images are representative for 8 visualized cell divisions. Horizontal scalebar indicates 1 μm and the vertical scalebar indicates 5 min. (F) (Related to Figure 3G) Transmission electron micrographs of cross walls in Δ*kin4-Ia* and Δ*kin4-Ic* mutant cells. An enlarged view of the boxed areas is shown on the right. Irregular protrusions from the cross walls are marked with an arrow. Compare with Figure 3G. Scalebars indicate 5 μm in the left images and 1 μm in the enlarged views. (G) Table showing quantification of the number of cross walls with a structural defect. A defect was defined as a local protrusion in the cross wall with a length at least 0.5 times the thickness of the cross wall, as exemplified in F. Defects were recorded separately in the centre of the cross wall and at the T-shaped junctions between the cross wall and maternal cell wall that represent the former attachment sites of the cell plate.

Supplemental Experimental Procedures

Plasmids and cloning procedures

All plasmids used were generated using standard restriction-ligation cloning procedures and were verified by sequencing. The use of plasmids and primers is summarized in the two lists below.

List of primers used in this study

Primer	Use	Sequence (5' > 3')	RE site
TM227	Cloning of GFP/mCherry fluorophore	ATAAGCTTGATATCTTGGTGAGCAAGGGCGAGGAGCTG	*Hind*III
JK74	Cloning of GFP/mCherry fluorophore	AGGAATTCTTACTTGTACAGCTCGTCCATGC	*Eco*RI
JK117	Cloning of nopaline synthase terminator	GCGAATTCCTACAGCCCCGAAATAAC	*Eco*RI
JK118	Cloning of nopaline synthase terminator	AACTGCAGCTCATGTTTGACAGCTTATCATCGG	*Pst*I
JK138	Cloning of SCAMP4 left targeting arm	CCGCTCGAGGCCAAAACATGGAAACCTACCTTAGG	*Xho*I
JK139	Cloning of SCAMP4 left targeting arm	CCCAAGCTTGATAGCTACTCTGCTTGCTGCAGC	*Hind*III
JK140	Cloning of SCAMP4 right targeting arm	GCTCTAGATTTTACTGTATTCTTATTGTTAGTTGAGG	*Xba*I
JK141	Cloning of SCAMP4 right targeting arm	CGCGAGCTCCATCATACCACTTCTCAAACACATGC	*Sac*I
Kin4-Ic-5' UTR Fw	Cloning of Kin4-Ic KO left targeting arm	AAAGGTACCGCCAAGGAGCAAAGATACACGGCTG	*Kpn*I
Kin4-Ic-5' UTR Rv	Cloning of Kin4-Ic KO left targeting arm	AAACTCGAGCGTCGCTACTAATGTACACCCAGC	*Xho*I
Kin4-Ic-3' UTR Fw	Cloning of Kin4-Ic KO right targeting arm	AAACATATGCATTTGTGGGGTTCAACCTGAGC	*Nde*I
Kin4-Ic-3' UTR Rv	Cloning of Kin4-Ic KO right targeting arm	AAACCGCGGGAAGATTCAAAAAGGTTAGC	*Sac*II
JK198	Cloning of Kin4-Ia KO left targeting arm	GGGGTACCTGAAATCGAGATATGGCAGCAGC	*Kpn*I
JK199	Cloning of Kin4-Ia KO left targeting arm	CCGCTCGAGTTGTGCACTGATTTGTGAATCAAGTG	*Xho*I
JK234	Cloning of Kin4-Ic motor domain	CATGCCATGGGAGCAGACAAAGCAAACG	*Nco*I
JK235	Cloning of Kin4-Ic motor domain	AGAAGCGGCCGCTCCGTTAGGAGCAGTATCTTTAGACG	*Not*I
JK220	SCAMP4 GFP/mCherry tagging genotyping	GTGATCAACGTGGGATTAAAGAAGTCAC	-
JK206	Kin4-Ia deletion genotyping	TTTGAGGTGTATCACCCAGTTTCG	-
JK207	Kin4-Ia citrine tagging genotyping	GGAGGAAAGTGATGGCGAAAGAGC	-
JK208	Kin4-Ia deletion / citrine tagging genotyping	GCAGGAAGCACGAGCTAAGACC	-
JK221	Kin4-Ia gene specific primer - begin	GTTGAGACGCTGAAGGACAGTGC	-
JK222	Kin4-Ia gene specific primer - begin	CCAGCCAAGTCAACAAGGTGAAGC	-
JK223	Kin4-Ia gene specific primer - end	GCAGAATTGGTTGGAACAGGAGC	-
JK224	Kin4-Ia gene specific primer - end	TCCACATCTCGCCTCTTCACAGC	-
JK209	Kin4-Ic deletion genotyping	CAGAAAGTGCCGAATGCGCTCC	-
JK210	Kin4-Ic citrine tagging genotyping	ACTGACCTGCCACATTCCGAGC	-
JK211	Kin4-Ic deletion / citrine tagging genotyping	TTGACTTGTGTGGAATCTTGGATGC	-
JK212	Kin4-Ic gene specific primer - begin	CCTACCACAATGGGCAAACCTCC	-
JK213	Kin4-Ic gene specific primer - begin	GCGTTTGAGTCTGCTGGGCTTAC	-
JK214	Kin4-Ic gene specific primer - end	GACCCTCTTGCACCTCATGTTTGG	-
JK215	Kin4-Ic gene specific primer - end	GAATGTGGCAGGTCAGTGCTCG	-
JK130	Primer on resistance cassettes forward	TGCTAAGGCAGGGTTGGTTACG	-
JK160	Primer on resistance cassettes reverse	TGCGAAGGATAGTGGGATTGTGC	-
JK125	Sequencing of terminator after mCherry	AGAGGCTGAAGCTGAAGGACG	-
JK129	Sequencing region upstream of mCherry	CCCTTGGTCACCTTCAGCTTGG	-
JK112	Sequencing region upstream of GFP	GCCGGACACGCTGAACTTGTG	-
JK114	Sequence downstream of resisistance cassette	ACTCAAGAGGATAAAACCTCACC	-
JK111	Construct sequencing general	GATTAAGTTGGGTAACGCCAGG	-
JK116	Construct sequencing general	ACACAGGAAACAGCTATGACC	-
JK236	Sequencing of pET28a-Kin4-Ic-(794)	GCGAAATTAATACGACTCACTATAGGG	-
JK237	Sequencing of pET28a-Kin4-Ic-(794)	GCTAGTTATTGCTCAGCGGTGG	-
JK238	Sequencing of pET28a-Kin4-Ic-(794)	CTACCACAATGGGCAAACCTCC	-
JK239	Sequencing of pET28a-Kin4-Ic-(794)	AGCCTACGGTCAATCGAGATCC	-

List of plasmids used in this study

Plasmid	Usage	Source
pTM374	C-terminal citrine tagging of Kin4-Ia	[S5]
pTM365	C-terminal citrine tagging of Kin4-Ic	[S5]
pmCherry-LoxP-BsdR	Vector for making c-terminal mCherry fusion proteins at an endogenous locus; Blasticidin resistance	This study
peGFP-nptII	Vector for making c-terminal GFP fusion proteins at an endogenous locus; G418 resistance	This study
SCAMP4-mCherry	C-terminal mCherry tagging of SCAMP4	This study
SCAMP4-GFP	C-terminal GFP tagging of SCAMP4	This study
Kin4-Ic-KO-HygR	Knock-out of the entire Kin4-Ic reading frame	This study
Kin4-Ia-KO-HygR	Knock-out of the entire Kin4-Ia reading frame; Hygromycin resistance	This study
Kin4-Ia-KO-NatR	Knock-out of the entire Kin4-Ia reading frame; Nourseothricin resistance	This study
MAP65a-mCherry	C-terminal mCherry tagging of MAP65a	This study
pET28a-Kin4-Ic-(794)	Bacterial production of N-terminal Kin4-Ic fragment	This study

pmCherry-LoxP-BsdR

First, the sequence encoding the citrine fluorophore in pCTRN-nptII [S2] was exchanged for that of mCherry using a fragment amplified with primers TM227 and JK74 and introduced using *Hind*III and *Eco*RI sites. Next, the nopaline synthase terminator (Tnos) and nptII resistance cassette were removed using *Bam*HI and *Eco*RI. Finally, the blasticidin resistance cassette, obtained from p35S-loxP-BsdR (AB537973) as a *Pst*I / *Bam*HI fragment, and Tnos, obtained as a PCR fragment amplified from pCTRN-nptII using JK117 and JK118 and digested with *Eco*RI and *Pst*I, were introduced.

peGFP-nptII

The citrine fluorophore encoding sequence in pCTRN-nptII was exchanged for that of eGFP amplified with primers TM227 and JK74 using *Hind*III and *Eco*RI sites.

SCAMP4-mCherry

A ~0.7 kb region of the 3' end of the SCAMP4 gene and a ~1.1 kb region downstream of the stop codon were amplified using primers JK138 till JK141 and cloned into pmCherry-LoxP-BsdR using *Xho*I / *Hind*III and *Xba*I / *Sac*I sites.

SCAMP4-GFP

The mCherry fluorophore coding sequence and blasticidin resistance cassette were removed from SCAMP4-mCherry and replaced with eGFP and the nptII resistance cassette obtained from peGFP-nptII using *Hind*III and *Xba*I sites.

Kin4-Ic-KO-HygR

A ~0.8 kb region upstream the initiation codon of the Kin4-Ic gene and a ~1.0 kb region downstream of the stop codon were amplified using primers Kin4-Ic-5' UTR Fw, Kin4-Ic-5' UTR Rv, Kin4-Ic-3' UTR Fw and Kin4-Ic-3' UTR Rv and cloned into p35S-loxP-BsdR (AB537973) using *Kpn*I / *Xho*I and *Nde*I / *Sac*II sites. The blasticidin resistance cassette was subsequently replaced with the hygromycin resistance cassette from p35S-LoxP-HygR (pTN186) using *Xho*I and *Xba*I.

Kin4-Ia-KO-HygR

The ~1.0kb region after the stop codon of Kin4-Ia was obtained from pTM374 as a *Bam*HI / *Sac*I fragment and inserted into p35S-LoxP-HygR (pTN186). A ~1.0 kb region upstream of the start codon, amplified using primers JK198 and JK199 was subsequently introduced using *Kpn*I and *Xho*I.

Kin4-Ia-KO-NatR

The hygromycin resistance cassette of Kin4-Ia-KO-HygR was replaced with the nourseothricin resistance cassette from the γ-tubulin-a-KO plasmid [S3] using *Eco*RV, *Bam*HI and *Sac*I.

MAP65a-mCherry

The sequence encoding the citrine fluorophore and nptII resistance cassette in the MAP65a-citrine plasmid [S4] was replaced with that encoding mCherry and the blasticidin resistance cassette from pmCherry-LoxP-BsdR using *Cla*I and *Not*I.

pET28a-Kin4-Ic-(794)

The sequence encoding the first 794 amino acids of Kin4-Ic was PCR amplified from a cDNA library generated from *P. patens* protonemal tissue using primers JK234 and JK235. The resulting product was digested with *Nco*I and *Not*I and subsequently ligated into pET28a.

***P. patens* growth conditions and transformation**

P. patens tissues were grown on BCDAT plates under continuous light, unless stated otherwise. Plasmids were linearized and introduced into the *P. patens* genome by homologous recombination using PEG-mediated protoplast transformation [S6]. Correct insertion events were characterised by PCR. A summary of the characteristics of generated moss lines and their use throughout the study are listed below. For imaging, protonemal tissue was grown on BCD medium in glass bottom dishes [S6].

List summarizing moss strain characteristics and usage

Name	Experimental use	Main clone	Background strain	Plasmid transformed	Figure	Video	Source
MAP65a-citrine	Kinesin-4 knock-out construction	#2	WT	see reference	2, 3F-G, S1, S2C-D, S4B-C, S4G	S2	[S4]
MAP65c-citrine	Overlap / FM4-64 colocalization	#5	WT	see reference	1B	S1	[S4]
Δ*kin4-Ia*	Measuring effect of Kinesin-4 removal on overlap dimension	#7	MAP65a-citrine	Kin4-Ia-KO-HygR	2, 3F, S1, S2C-D, S4F-G	S2	This study
Δ*kin4-Ic*	Measuring effect of Kinesin-4 removal on overlap dimension	#172	MAP65a-citrine	Kin4-Ic-KO-HygR	2, 3F, S1, S2C-D, S4F-G	S2	This study
Δ*kin4-Ia* / Δ*kin4-Ic*	Measuring effect of Kinesin-4 removal on overlap dimension	#66	Δ*kin4-Ic*	Kin4-Ia-KO-NatR	2, 3E-G, S1, S2C-D, S4B-C, S4G	S2, S3	This study
SCAMP4-GFP	Validation of SCAMP4 as cell plate membrane marker	#42	WT	SCAMP4-mCherry	S3C-E	-	This study
SCAMP4-mCh	Cell plate membrane / overlap colocalization	#173	MAP65c-citrine	SCAMP4-mCherry	3A-D, S3C, S4A	S4	This study
Δ*kin4-Ic* / SCAMP4-mCh	Generating Kinesin-4 double mutant with membrane marker	#44	Δ*kin4-Ic*	SCAMP4-mCherry	S1A, S3C	-	This study
Δ*kin4-Ia* / Δ*kin4-Ic* / SCAMP4-mCh	Cell plate membrane / overlap colocalization in Kin-4 double mutant	#391	Δ*kin4-Ic* / SCAMP4-mCh	Kin4-Ia-KO-NatR	3A-D, S1A, S4A	S4	This study
Kin4-Ia-citrine	Intensity analysis of Kin4-Ia throughout cytokinesis	#43	WT	pTM374	S1C, S2A-B	-	This study; [S5]
Kin4-Ic-citrine	Intensity analysis of Kin4-Ic throughout cytokinesis	#57	WT	pTM365	S1C, S2A-B	-	This study; [S5]
Kin4-Ic-citrine / MAP65a-mCh	Kinesin-4 / overlap colocalization	#140	Kin4-Ic-citrine	MAP65a-mCh	S4D-E	-	This study

Recombinant protein production

An N-terminal, his-tagged fragment comprising the motor domain and coiled-coil regions required for dimerization of Kin4-Ic was produced in *E. coli* Rosetta2 (DE3) cells harbouring the pET28a-Kin4-Ic-(794) plasmid. Production was triggered through the addition of 0.2 mM IPTG and performed at 18 °C for 20 hours. Cells were lysed using a French press in a phosphate buffer (50mM NaH_2PO_4, 250mM NaCl, 10% w/v glycerol, pH 7.4), containing a protease inhibitor cocktail (Roche diagnostics), DNAseI and 30mM imidazole. After centrifugation the clarified lysate was incubated with Ni-NTA agarose beads (Qiagen) at 4°C for 1 hour. Beads were washed five times with phosphate buffer containing DNAseI and 30mM imidazole. Proteins were eluted in phosphate buffer containing 500mM imidazole in 1 mL fractions. The second fraction was aliquoted, flash frozen in liquid nitrogen and stored at -80 °C. Protein concentration was determined using coomassie staining of the purified protein on an SDS-PAGE gel including a BSA reference and subsequent densitometry of the bands (Figure S2E). Used concentrations refer to Kin4-Ic monomers.

Preparation of microtubule seeds
To prepare stabilized seeds, 10 µL of MRB80 (80 mM PIPES, pH 6.8, 1 mM EGTA, 4 mM $MgCl_2$) containing 0.4 µM Alexa 568-tubulin, 0.3 µM biotin-tubulin and 15.3 µM unlabelled tubulin was polymerised at 37 °C in the presence of 1 mM GMPCPP (guanosine-5'-[(α,β)-methyleno]triphosphate) for 30 minutes. Seeds were then pelleted using an airfuge (Beckman Coulter) operated at ~22 psi for 5 min, resuspended in 90 µL of MRB80 and stored at room temperature.

Glass treatment
Coverslips for microtubule polymerisation assays were first cleaned in acetone for 30 minutes and then with a solution composed of 10% (w/v) KOH mixed with isopropanol in a 2:1 ratio for 1 hour. It was subsequently silanized using a solution of 4.81 mM dichlorodimethylsilane (DDS) dissolved in trichloroethylene and washed twice in ethanol.

***In vitro* microtubule growth assays**
Microtubule growth assays were performed in flow chambers consisting of DDS-treated coverglass mounted on a glass slide separated by thin layer of silicone vacuum grease. This generated a small channel with a typical volume of 8 µL. The channel was incubated with goat-anti-biotin (Sigma B3640) dissolved in PBS for 5 min and after being rinsed with PBS, blocked with 1% Pluronic F-127 in PBS for 1 hour. After flushing the channel with MRB80, GMPCPP-stabilized seeds were added. Unbound seeds were removed by flushing the channel with MRB80 supplemented with 80 mM KCl and 1 mg/mL casein. Finally, 20 µL of assay buffer was introduced, consisting of MRB80 with 80 mM KCl, 1 mg/mL casein, 1 mM ATP, 1 mM GTP, 16.67 µg/mL catalase (Sigma), 33.33 mM D-glucose, 166.7 µg/mL glucose oxidase (Sigma), 0.45 µM Alexa 568-tubulin, 21.2 µM unlabelled tubulin (Cytoskeleton inc.) and the indicated amount of Kin4-Ic-(794). The sample was then transferred to a TIRF microscope for observation where it was kept at 30 ±1 °C using an objective heater.

Analysis of microtubule growth velocities
The growth velocities for a given experimental condition were determined by kymograph analysis. The catastrophe frequencies were determined by dividing the total number of observed catastrophe events by the total time microtubules spend in the growth phase. The error of the catastrophe rate was calculated by dividing the catastrophe rate by the square root of the number of observations [S7].

Fluorescence microscopy and staining
All live cell imaging was performed on a Roper spinning disc microscope composed of a Nikon Ti eclipse body, 100x Plan Apo VC objective (NA 1.40), Evolve 512 camera (Photometrics), Yokogawa CSU-X1 spinning disc head with a 1.2x post-magnification lens fitted between the spinning disc unit and the camera. Excitation light for citrine and GFP probes was provided by a 491 nm Cobolt Calypso50 laser and emitted light was filtered with a 527/60 bandpass filter (Semrock). For FM4-64 and mCherry probes a 561 nm Cobolt Jive50 laser line was used and emission light was filtered through a 595/50 bandpass filter (Chroma). Typical exposures were 500-700 ms for citrine, GFP and FM4-64 and 800-1000 ms for mCherry.
FM4-64 was dissolved in dH_2O and used at a final concentration of 10 µM. The dye was added to dividing cells at the moment of nuclear envelope breakdown, which is roughly 10 min before anaphase onset [S4].
Aniline Blue was used at a final concentration of 0.1% (w/v) in 0.1M K_2HPO_4. Tissue fixed in 2% (w/v) paraformaldehyde and 0.025% (v/v) glutaraldehyde was stained for 20-30 minutes after which it was rinsed twice with 0.1M K_2HPO_4 and mounted in the same solution for observation.
For imaging of the *in vitro* microtubule growth assay a TIRF setup was used. This consisted of a Nikon Ti eclipse microscope body equipped with a 100x Apo TIRF objective (NA 1.49) and a QuantEM 512SC camera (Photometrics). Excitation light was provided by a Cobolt Jive50 561 nm laser line and emission light was filtered using a 607/36 bandpass filter. An exposure time of 300 ms was used to acquire images at 5s intervals.

Differential interference contrast (DIC) microscopy
DIC microscopy was performed on a Nikon Ti eclipse microscope equipped with Normarski optics using a long working distance condenser (NA 0.52) and 100x Plan Apo VC objective (NA 1.40). Illumination was supplied by a CoolLED pE-100 light source. The lid of the glass bottom dish was removed before imaging and the sample was rotated such that the forming cell plate was perpendicular to the prism shear axis. Images were captured using an Andor iXon3 camera. The MAP65a-citrine signal was subsequently recorded using spinning disc microscopy essentially as described above.

Transmission electron microscopy
For transmission electron microscopy of protonemal cells, small fragments of protonemal tissue grown on BCD agar plates overlaid with cellophane were fixed in 0.1M sodium phosphate buffer (pH 7.4) containing 2.5% (v/v) glutaraldehyde, 0.5% (w/v) paraformaldehyde and 0.001% (v/v) triton x-100. Samples were postfixed in 1% (w/v) osmium tetroxide in phosphate buffer, dehydrated in a graded series of ethanol and subsequently embedded in Spurr low-viscosity embedding resin (Sigma EM0300). Ultrathin sections (~90 nm) were made and observed with a JEOL JEM1011 transmission electron microscope operated at an acceleration voltage of 80 kV.

Image analysis
All image analysis was performed using ImageJ and in-house developed Matlab (Mathworks) code, available on request.
The moment of anaphase onset in time lapse movies of mitotic events was determined either using direct observation of chromosome

separation or, when chromosomes could not be distinguished, using the rise in MAP65 midplane labelling intensity. The latter method was validated in a strain expressing both GFP labelled MAP65 and a histone-mRFP chromosome marker (data not shown).
To generate average intensity profiles of MAP65a-citrine or SCAMP4-mCherry perpendicular to the forming cell plate, the images were rotated (bicubic interpolation) such that the division plane was oriented vertically with the growing tip of the cell located on the right hand side. The gradual tilting of the division plane common in caulonemal cells, was countered using the ImageJ StackReg plugin (Rigid body type translation). The signal of the division plane was isolated from the remainder of the image using automated thresholding based on the maximum entropy method. The centre of the intensity distribution in each horizontal line of the thresholded area was then calculated using intensity-weighted averaging. The calculated centres were used to align the horizontal lines which were finally averaged along the vertical axis. To generate kymographs displaying the evolution of the intensity profiles for MAP65 (Figure 2B), the profiles were normalized to the brightest pixel.
Velocities of radial expansion were obtained by kymograph analysis of StackReg-treated movies (see above). A line following the division plane was used for generating a kymograph of the MAP65a-citrine signal. The steepness of the two shoulders present in the resultant kymograph were then used to calculate the velocity of lateral expansion.
The average thickness of the cross walls observed using transmission electron microscopy was calculated by dividing the surface area of the cross wall by the length of the cross wall.

Statistical data analysis
For statistical validation, data were first tested for normality using the Shapiro–Wilk test (<50 samples) or Kolmogorov–Smirnov test (≥50 samples). When normality was assumed ($P>0.05$), data were evaluated using unpaired *t*-tests. For data where a normal distribution was not assumed, Mann-Whitney U and Kruskal-Wallis tests were employed.

Supplemental References

[S1] Law, A.H.Y., Chow, C.M., and Jiang, L. (2012). Secretory carrier membrane proteins. Protoplasma *249*, 269–283.

[S2] Hiwatashi, Y., Obara, M., Sato, Y., Fujita, T., Murata, T., and Hasebe, M. (2008). Kinesins are indispensable for interdigitation of phragmoplast microtubules in the moss *Physcomitrella patens*. Plant Cell *20*, 3094–3106.

[S3] Nakaoka, Y., Kimura, A., Tani, T., and Goshima, G. (2015). Cytoplasmic nucleation and atypical branching nucleation generate endoplasmic microtubules in *Physcomitrella patens*. Plant Cell *27*, 228–242.

[S4] Kosetsu, K., de Keijzer, J., Janson, M.E., and Goshima, G. (2013). MICROTUBULE-ASSOCIATED PROTEIN65 is essential for maintenance of phragmoplast bipolarity and formation of the cell plate in *Physcomitrella patens*. Plant Cell *25*. 4479–4492.

[S5] Miki, T., Naito, H., Nishina, M., and Goshima, G. (2014). Endogenous localizome identifies 43 mitotic kinesins in a plant cell. Proc. Natl. Acad. Sci. USA *111*, E1053–E1061.

[S6] Yamada, M., Miki, T., and Goshima, G. (2016) Imaging mitosis in the moss *Physcomitrella patens*. In Methods in Molecular Biology, vol. 1413, P. Chang and R. Ohi eds. (United States: Springer), pp. 263–282.

[S7] Walker, R.A., O'Brien, E.T., Pryer, N.K., Soboeiro, M.F., Voter, W.A., Erickson, H.P., and Salmon, E.D. (1988). Dynamic instability of individual microtubules analyzed by video light microscopy: rate constants and transition frequencies. J. Cell Biol. *107*, 1437–1448.